

# A 3D Reconstruction Benchmark for Asset Inspection

James L. Gray , Nikolai Goncharov , Alexandre Cardaillac , Ryan Griffiths , Jack Naylor , and Donald G. Dansereau 

Australian Centre for Robotics, School of Aerospace, Mechanical and Mechatronic Engineering, University of Sydney, Sydney, NSW, Australia  
{james.gray1, nikolai.goncharov, alexandre.cardaillac, r.griffiths, jack.naylor, donald.dansereau}@sydney.edu.au

**Abstract.** Asset management requires accurate 3D models to inform the maintenance, repair, and assessment of buildings, maritime vessels, and other key structures as they age. These downstream applications rely on high-fidelity models produced from aerial surveys in close proximity to the asset, enabling operators to locate and characterise deterioration or damage and plan repairs. Captured images typically have high overlap between adjacent camera poses, sufficient detail at millimetre scale, and challenging visual appearances such as reflections and transparency. However, existing 3D reconstruction datasets lack examples of these conditions, making it difficult to benchmark methods for this task. We present a new dataset with ground truth depth maps, camera poses, and mesh models of three synthetic scenes with simulated inspection trajectories and varying levels of surface condition on non-Lambertian scene content. We evaluate state-of-the-art reconstruction methods on this dataset. Our results demonstrate that current approaches struggle significantly with the dense capture trajectories and complex surface conditions inherent to this domain, exposing a critical scalability gap and pointing toward new research directions for deployable 3D reconstruction in asset inspection. Project page: <https://roboticimaging.org/Projects/asset-inspection-dataset/>

**Keywords:** 3D reconstruction · asset inspection · detail imaging

## 1 Introduction

3D reconstruction is the task of building a three-dimensional model of the scene from sensor data, such as LIDAR and/or RGB cameras. Using RGB cameras has significant advantages in terms of cost and convenience, and they allow the 3D model to actually take on the appearance of the scene. One key application of 3D reconstruction is in asset inspection and management. In this case, one can take many photos of an asset (often with a drone) and a 3D reconstruction approach can then be used to build a digital twin of the asset for remote inspection. Building a digital twin of the asset can provide users with an intuitive way to

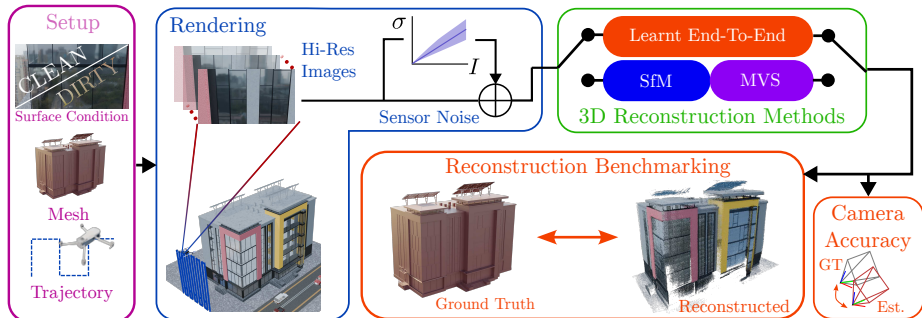


**Fig. 1:** We propose a new benchmark for 3D reconstruction from imagery captured in asset inspection operations. Given user-specified surface soiling, drone trajectories and asset meshes, we generate synthetic data using Blender [3] that matches the close proximity and high overlap of data captured in industrial asset inspection operations. After adding emulated signal-dependent sensor noise, we benchmark the camera pose and 3D reconstruction accuracy of both end-to-end transformer architectures and traditional structure from motion and multi-view stereo pipelines with ground truth data from our simulator.

navigate through the vast numbers of photos and can be used to find defects or areas that need maintenance [25, 42].

Significant recent progress has been made in the field of 3D reconstruction. New end-to-end (E2E) learning-based models offer excellent accuracy, such as [28, 52, 57]. At the same time, advances have been made in structure from motion (SfM) and multi-view stereo (MVS) have yielded significant improvements in efficiency [36] and in accuracy [5, 61]. This has been partially driven by the availability of datasets and benchmarks such as [19, 24, 40, 60], which allow quantitative evaluation of methods. However, for the purposes of evaluating the 3D reconstruction performance of a method on asset inspection data, these benchmarks have several limitations. These datasets contain many images of an object captured with significant overlap between views, often with one whole side of the object visible in each view. On the other hand, asset-inspection photos are typically taken with an emphasis on detail, aiming for 1.5mm to 10mm per pixel of resolution [46, 48]. To our knowledge, there is no publicly-available dataset that contains images entirely captured in this pattern. As a result, there exists a domain gap between the existing 3D reconstruction datasets in the research literature used to evaluate 3D reconstruction methods and a key application for their use.

Another limitation of several existing datasets and benchmarks is that most only provide ground truth mesh or point clouds and camera poses [19, 24, 32]. Others only provide sparse ground truth depth maps [40]. With these datasets, it is possible to evaluate a method’s global end-to-end performance and camera pose estimation. However, point cloud accuracy metrics are global measures that

may obscure local geometric errors, which is a critical consideration in asset inspection contexts.

3D reconstruction methods often perform worse in visually complex environments, such as those with reflective and transparent surfaces [16, 18]. This is particularly relevant for buildings with glass facades, a commonly inspected asset class. Some datasets include reflective objects, such as ShinyBlender [50] and PASMVS [4]. However, none isolate changes in surface condition, due to factors such as dirt and scratches, from geometry. Yet, surface condition significantly affects photometric consistency and reconstruction performance, making this an important consideration for benchmarking.

To address the limitations of existing datasets and benchmarks in an asset inspection context, this paper presents three key contributions:

1. A new rendered dataset that follows an asset inspection style capture pattern, with ground truth depth maps, camera poses, and a 3D mesh for each scene. One scene in this dataset provides varying levels of soiling on its windows to allow one to isolate the impact of surface condition on 3D reconstruction performance.
2. An open source pipeline to allow one to recreate, modify and/or extend this dataset.
3. An evaluation of a representative selection of prominent state-of-the-art 3D reconstruction methods on this new dataset, including end-to-end, structure from motion and multi-view stereo methods.

By leveraging Blender within our synthetic data generation pipeline, we simulate realistic inspection challenges while maintaining control over the scene parameters. Through the release of this targeted dataset, our open-source generation pipeline, and a comprehensive evaluation of state-of-the-art techniques, we aim to provide the community with the tools necessary to develop, rigorously test, and advance 3D reconstruction methods for the demanding requirements of industrial asset inspection.

A link to the dataset is included in the supplementary material.

## 2 Related Work

### 2.1 3D Reconstruction Methods

Traditionally, 3D reconstruction from a series of 2D images with unknown camera poses is performed through the combination of two methods: SfM to recover sparse points, camera pose and intrinsics, and MVS to reconstruct a dense point cloud of the scene. The SfM pipelines find correspondences between images [31, 37] and triangulate 3D points using the epipolar geometry of calibrated camera models [17]. COLMAP [38] introduced an incremental reconstruction approach that substantially improved robustness, accuracy, and scalability over previous methods [6, 44], introducing next-best view selection and robust triangulation of 3D points. Recently, improvements to problem initialisation and

principled formulation of global SfM optimisation in GLOMAP [36] has achieved on-par or superior accuracy while substantially improving speed over incremental approaches [38]. Lindenberger et al. [30] proposed using dense feature maps derived from deep neural networks to fine-tune poses at the sub-pixel level, leading to substantially improved reconstruction quality and pose accuracy.

After SfM, images are passed into an MVS pipeline [11,12,62] which matches regions of images to produce dense 3D point clouds. Schönberger et al. [39] introduced a novel view selection algorithm, integrated into COLMAP [38] that prioritises photometric and geometric consistency and smoothness to produce robust and efficient dense reconstructions. In non-Lambertian regions, these algorithms generally fail, giving incorrect surface reconstructions, and all such approaches struggle in scenes with large textureless or non-Lambertian regions like those present in asset inspection operations.

More recently, end-to-end learning-based approaches incorporating large-scale labelled data [56] have provided a compelling alternative. These approaches leverage transformer-based architectures and pre-training with existing large-scale 3D reconstruction datasets to produce accurate point maps from unconstrained image collections, even with little overlap between frames and in the presence of complex appearances. Subsequent work extended this to enable dense image matching in 3D [26] and an end-to-end learnt SfM pipeline [7] with refinement via gradient descent. VGGT [52] introduces an architecture that separately predicts cameras and dense products, including depth maps, point maps, and point tracks, performing well even in regions with little inter-frame overlap.  $\pi^3$  [57] extends this paradigm with a permutation-invariant architecture, scale-invariant geometry, and affine-invariant camera poses, which improves robustness and accuracy by avoiding explicit reference frames. Depth Anything 3 [28] takes a complementary approach through monocular depth estimation, producing per-frame depth maps without requiring multi-view consistency, providing a strong baseline for dense scene recovery without explicit pose estimation. These approaches produce reconstructions of equal or improved quality compared to traditional approaches, with key benefits in non-Lambertian regions; however, their applicability to close-proximity, high-overlap datasets characteristic of asset inspection has not been investigated. In this work, we evaluate both state-of-the-art learning-based methods, including VGGT,  $\pi^3$  and Depth Anything 3 (DA3), and traditional benchmark approaches COLMAP and GLOMAP on this new dataset, identifying where open challenges remain.

## 2.2 Reconstruction for Asset Management

Increasingly, aerial platforms are used to survey and inspect assets [34,59], with imagery used to produce detailed 3D models and inform maintenance and repair decisions. Trajectory planning for asset reconstruction has received attention [8,9], although the focus is largely on large-scale completeness rather than fine surface detail required in asset management tasks [58]. Smith et al. [43] introduce a framework benchmarking 3D reconstruction from different trajectory

**Table 1:** Comparison between our dataset and existing 3D reconstruction and drone imagery datasets. This table compares whether each dataset is captured in an asset inspection style, whether varying levels of surface condition (reflectivity or smudging in our case) are present with the same geometry and what ground truth data is available. Note, Cam. refers to camera parameters. Scenes with an asterisk have variable lighting or environmental conditions.

Dataset	Captured	Inspection	Surfaces	Depth	Cam.	3D Data	Scenes
ETH3D [40]	✓	✗	✗	Sparse	✓	✓	25
Urban SaR [32]	✓	✗	✗	✗	✗	✓	2
PASMVS [4]	✗	✗	✓	✓	✓	✗	400
BlendedMVS [60]	✗	✗	✗	✗	✓	✗	110k
DTU [19]	✓	✗	✗	✗	✓	✓	140
ClaraVid [2]	✗	✗	✗	✓	✓	✓	40
MatrixCity [27]	✗	✗	✗	✓	✓	✓	1*
LightCity [54]	✗	✗	✗	✓	✓	✓	1*
UrbanScene3D [29]	✓	✗	✗	✓	✓	✓	16
Smith et al. [43]	✗	✗	✗	✗	✓	✓	5
<b>Ours</b>	✗	✓	✓	✓	✓	✓	3

plans, demonstrating higher completeness and improved reconstruction from optimised per-scene trajectories, motivating structured evaluation of reconstruction quality under controlled scene capture conditions. In this work, we introduce a rendering pipeline where new datasets may be generated from user-defined trajectories with control over scene parameters, including the surface condition of non-Lambertian elements, enabling benchmarking across a wide array of 3D reconstruction pipelines.

Neural scene representations including NeRF [33] and Gaussian Splatting [22] have found increasing application in asset reconstruction [20, 47]. Extensions targeting non-Lambertian surfaces [15, 16, 21, 23, 35, 50] show particular promise for photorealistic reconstruction of challenging appearances. However, all such methods remain dependent on the accuracy of upstream pose and geometry estimates from SfM pipelines; therefore, improvements to reconstruction quality propagate directly into the fidelity of these derived representations [36]. This motivates rigorous benchmarking of the underlying 3D reconstruction methods in inspection-relevant conditions, which this work directly addresses.

### 2.3 Datasets

Several existing datasets have been introduced to benchmark 3D reconstruction approaches. In many cases, this focuses on large-scale ground-captured scenes [24, 45] or object-level scenes [19, 41] as opposed to those from aerial platforms. ETH3D [40] is a captured dataset with high-resolution image data, LiDAR point clouds for ground truth and estimated camera motion. While it is of high resolution, given the proximity to buildings and with five scenes of

reflective content, the dataset does not reflect the close proximity and structured capture conditions of asset management operations. BlendedMVS [60], UrbanScene3D [29] and UrbanSaR [32] all contain large-scale data with ground truth poses and scene point clouds; however, they are restricted to birds-eye view capture. While datasets targeted to novel view synthesis provide varying levels of specularly [4], lighting [27] and environmental [54] conditions, the impact of these effects is generally not considered when benchmarking traditional 3D reconstruction pipelines. While some works have considered multiple resolution scales [2] for complex scenes, targeted reconstruction from high-resolution close-proximity imagery is largely unexplored.

As shown in Table 1, few of these datasets contain ground truth depth maps and scene-level 3D data. Only PASMVS [4] intentionally benchmarks non-Lambertian appearance, and to our knowledge, no existing dataset contains close-proximity aerial data mimicking asset inspection operations. In this work, we provide a dataset of simulated scenes in a high-overlap, high-resolution capture scenario with varying surface conditions and ground truth 3D data to benchmark traditional and emerging 3D reconstruction techniques.

### 3 Asset Inspection Dataset

#### 3.1 Overview

This dataset consists of 3 scenes, *Office building*, *Crane* and *Bridge*. The models used for these scenes are referenced in the supplementary material. These are designed to simulate real-world structures that would undergo inspection. To mimic an asset-inspection style capture pattern, camera poses are kept close to each object, resulting in only a small portion of the object being visible in each view, as suggested in [46]. However, between each view, there is around an 80% overlap. Around the corners of objects, the camera makes smooth transitions between one side of the object and the other as suggested in [48]. Each image is captured with a simulated 50mm focal length and a sensor width of 36mm at 1920 x 1080 resolution to provide a high level of detail in each image, which is necessary in an asset-inspection application. Each scene has a ground truth mesh model, depth maps, and camera poses. This allows one to evaluate each stage in multi-stage methods, such as COLMAP, individually. Frames from each scene are included in the supplemental material.

*Office building* This scene has 4763 frames. It models a modern-day office building with large windowed areas that are highly reflective and large flat low-texture surfaces (see Fig. 2). This scene represents a significant challenge to 3D reconstruction approaches, which rely on Lambertian assumptions and the presence of distinctive features. To investigate the impact of reflectivity on reconstruction accuracy, the Office scene was rendered with 4 different surface condition settings (very low, low, medium, high) with the same geometry, thus isolating the effect of the reflections. These surface condition settings change the strength and amount of soiling on the windows as shown in Fig. 2.

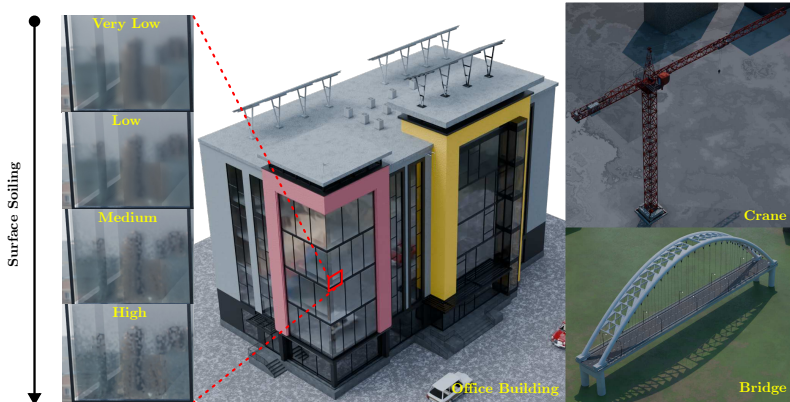


**Fig. 2:** Renders of the *office building*, *crane* and *bridge* scenes. The office scene was rendered with four surface conditions corresponding to very low, low, medium and high levels of soiling.

*Crane* This scene has 642 frames and simulates a construction crane with complex geometry, and mostly Lambertian surfaces (see Fig. 2). There are very few flat regions in this scene, presenting a significant challenge for methods that rely on planar assumptions. The truss structure of the crane is also highly repetitive, which can make it difficult for methods to localise the cameras and reconstruct the geometry of the truss.

*Bridge* This scene has 1074 frames and features an arch-bridge that suspends a road below via cables. The road has street lights and footpaths on either side (see Fig. 2). This scene is similar to the *Crane* scene because it has complex, but repetitive geometry and Lambertian surfaces. However, the geometry is comparatively simpler owing to the presence of large planar regions (*e.g.* the road and footpaths) and the arch and columns, which primarily consist of tubular structures.

### 3.2 Producing the Dataset

To generate a highly realistic synthetic dataset suitable for evaluating robust computer vision models and mapping approaches, we selected Blender [3], an open-source 3D creation suite with photorealistic rendering capabilities. The dataset was explicitly designed with asset inspection in mind and focuses on high-detail close-up viewpoints that approximate established industry inspection guidelines [46, 48]. A primary challenge in using synthetic data is the sim-to-real gap. To minimise this gap, the synthetic generation pipeline was continuously evaluated and refined by comparing the rendered images against actual asset inspection images. This ensured that the synthetic domain accurately simulated the complex lighting, scaling, and structural characteristics found in natural scenes.

Minimising the sim-to-real gap further required the intentional introduction of noise and imperfections, as synthetic renders inherently suffer from an artificially pristine appearance. Because the inspection views are captured at close ranges, maintaining realism dictated that materials possess sufficient, non-uniform details. To achieve this, most surface textures were procedurally generated to avoid the unrealistic repetition and self-similarity of tiled image textures. To ensure that the reflections properly simulate building windows, we added low-frequency noise into the normal maps of the windows, which warps the reflections a small amount. We also added a transparent component to the windows so that both the interior and the reflection were visible. Finally, we simulated a small amount of realistic sensor noise in the rendered images by adding random noise to the images during post-processing. Following [10], we model image noise as a combination of thermal and signal-dependent Poisson components to ensure simulation fidelity.

## 4 Benchmark Methods

We evaluate several methods, which are summarised in Tab. 2. These methods can be broadly divided into: transformer-based end-to-end models and pipelines consisting of a structure from motion stage and a subsequent multi-view stereo.

### 4.1 End-to-End Approaches

Transformer-based end-to-end models perform 3D reconstruction in a single forward pass, estimating depth maps, point clouds, camera, extrinsics and camera intrinsics from a series of images. We evaluate Depth Anything 3 [28], VGGT [52] and  $\pi^3$  [57] as current state-of-the-art approaches, which have been both benchmarked and trained on large-scale visual 3D reconstruction datasets [19, 40, 60]

A defining characteristic of asset inspection is the need for dense and continuous capture trajectories, which frequently result in thousands of high-resolution

**Table 2:** Comparison of evaluated methods. ✓ indicates required input and supported output while ✗ indicates unsupported inputs and outputs, and ~ refers to optional input. PC refers to dense pointcloud reconstructions and Intrin. and Extrin. are camera intrinsics and extrinsics respectively.

Method	Batch	Inputs		Outputs					
		Intrin.	Extrin.	Depth	Normal	PC	Intrin.	Extrin.	
E2E	DA3 [28]	400	~	~	✓	✗	✓	✓	✓
	VGGT [52]	200	✗	✗	✓	✗	✓	✓	✓
	$\pi^3$ [57]	100	✗	~	✓	✗	✓	✗	✓
SfM/MVS	COLMAP [38, 39]	All	~	~	✓	✓	✓	✓	✓
SfM	GLOMAP [36]	All	~	~	✗	✗	Sparse	✓	✓

images per asset. Current state-of-the-art end-to-end methods, namely Depth Anything 3, VGGT, and  $\pi^3$ , cannot process the full trajectories of these datasets natively due to large VRAM requirements on GPUs, highlighting a critical scalability gap in the current literature. To evaluate the capabilities of the models despite memory bottlenecks, we employ a decoupled batched evaluation strategy. We compose image sequences into unique sequential batches of  $N$  images (where  $N \in [100, 400]$ ), which are passed to each network.

Each batch possesses local frames and scales that need to be aligned into a global, consistent reference frame. We estimate a scale and local-to-global transform using a Sim(3) transform (rotation, translation and scale) [49] between the estimated and ground-truth trajectories using the evo toolbox [14] after outlier removal. In this case, we define outliers as being beyond a certain distance from the median camera pose. The resulting transform and scale are applied to the point cloud and all poses, aligning all batches into a consistent global frame and scale.

## 4.2 Structure from Motion and Multi-view Stereo

We evaluate two SfM pipelines: COLMAP [38], an incremental method widely used as a benchmark for 3D reconstruction, and GLOMAP [36], a global SfM approach designed to achieve comparable accuracy with improved scalability on large datasets. We first run the COLMAP automatic reconstruction in video mode, assuming a pinhole camera model and no distortion, to obtain a sparse reconstruction, and then run the COLMAP dense MVS on that sparse model to produce a dense reconstruction. Separately, we run GLOMAP for the SfM stage using the same features and matches extracted by COLMAP, producing an alternative sparse reconstruction. This yields three reconstructions: a COLMAP sparse SfM model, a COLMAP dense MVS model, and a GLOMAP sparse SfM model computed from COLMAP features and matches. Exact hyperparameters used in all experiments are provided in the supplementary material.

# 5 Evaluation

This section details the procedures (see Sec. 5.1) and metrics (see Sec. 5.2) that we use to evaluate the methods discussed in Sec. 4 and the results we obtain. The hardware used to perform this evaluation and the camera intrinsics results are detailed in the supplemental material.

## 5.1 Implementation Details

Comparing MVS methods, which require pre-computed camera parameters, with end-to-end approaches, which jointly estimate poses and geometry, is not straightforward. To ensure a fair comparison, we provide all methods with ground-truth camera parameters as a common baseline. We additionally evaluate end-to-end methods using their own estimated parameters, and MVS methods using COLMAP-estimated parameters, as COLMAP remains a standard in the field.

To compare the estimated point cloud with the ground truth mesh produced by Blender, we first sample the Blender mesh output to produce a point cloud.

During evaluation, we downsample ground truth depth maps to match the resolution of method outputs. While the intuitive approach is to apply a low-pass filter, as one would with an image, this is problematic because: depth maps do not necessarily exhibit band limited sampling properties [13]; filter-based methods propagate invalid regions (*e.g.* sky regions) throughout the depth map, and edges are not preserved. Therefore, we use nearest-neighbor downsampling to avoid these issues.

## 5.2 Metrics

We evaluate each method according to depth map accuracy, camera pose accuracy, and point cloud accuracy.

*Depth Maps* To evaluate depth maps, we use the scale-invariant mean squared error (sRMSE) as defined in [1].

*Camera Poses* To evaluate the camera poses, we use the area under curve (AUC) or mean average accuracy, as per [53]. Since some methods produce incomplete sets of poses if they have low certainty, we only evaluated valid estimated poses. For context, we also report the number of valid images as a proportion of the total images in the supplemental material.

*Point Clouds* To evaluate the estimated point clouds, we use the chamfer distance as per [28] and the F1-score defined in terms of accuracy and completeness metrics as per [51, 55, 57].

Note that our simple batching procedure discussed in Sec. 4, requires the use of ground truth information that would not be available in reality. Therefore, this evaluation focuses on performance metrics that can be estimated locally, such as depth map accuracy metrics. Furthermore, point cloud metrics that depend on estimated poses of batched methods are not directly comparable to non-batched methods and should be interpreted in this context.

## 5.3 Per-View Depth Reconstruction

We compare the performance of depth reconstruction per-view in Tab. 3. As soiling introduces more unique Lambertian content onto reflective surfaces in the scene, COLMAP’s accuracy improves. The end-to-end trained methods show both qualitative improvement, as seen in Fig. 3, and lower sRMSE values than COLMAP in these reflective scenes. For these pre-trained models, increasing soiling has little effect on reconstruction, only slightly increasing the sRMSE in the case of  $\pi^3$ . Except for VGGT, transformer-based methods demonstrate superior performance for both the *crane* and *bridge* scenes, and they more accurately predict depths for textureless regions and thin structures than COLMAP.

**Table 3:** Depth reconstruction accuracy measured as sRMSE ( $\downarrow$  better) for each scene. Here, Params refers to camera intrinsics and extrinsics. Depth Anything 3 outperforms the the other methods on all scenes except for *crane*.

		Office						
Method		V. Low	Low	Med.	High	Crane	Bridge	
E2E	DA3 (GT Params.)	<b>0.113</b>	<b>0.114</b>	<b>0.113</b>	<b>0.113</b>	0.207	<b>0.063</b>	
	DA3 (Est. Params.)	0.118	0.118	0.118	0.118	0.353	0.075	
	VGGT (Est. Params.)	0.200	0.199	0.199	0.201	<b>0.202</b>	0.837	
	$\pi^3$ (Est. Params.)	0.258	0.260	0.262	0.265	0.625	0.174	
MVS	COLMAP (GT Params.)	0.574	0.576	0.570	0.547	1.496	0.755	
	COLMAP (GLOMAP Params.)	0.407	0.407	0.415	0.396	1.482	0.863	

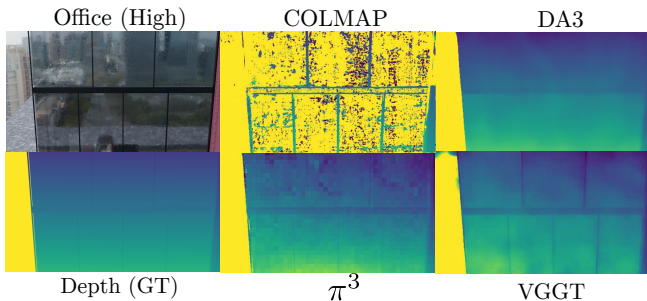


**Fig. 3:** Depth maps rendered on the *office building* (high) scene using self-estimated camera parameters. Each depth map is scaled to match the ground truth range, with near-far corresponding to blue-yellow. Learning-based approaches demonstrate superior performance even in the case of high soiling on reflective scene content, despite recovering less accurate poses. COLMAP is unable to accurately match large regions of non-Lambertian scene content, commonly seen in asset inspection tasks.

## 5.4 Camera Pose Recovery

We evaluate the accuracy of estimated camera poses quantitatively in Tab. 4 and qualitatively in Fig. 4. From these results, we can see that most methods perform quite poorly on this dataset. All the transformer-based methods, except for Depth Anything 3, achieve very low AUC scores. Even the highest performing method, Depth Anything 3, still produces a relatively low AUC score compared to its results on other datasets. Note that these methods perform well in scenes with similar structures when each view has longer sight lines and captures more of the scene [28, 52, 57]. This suggests that many transformer-based learning approaches are not well-suited for asset inspection, where only a small portion of the object is visible in each view. All methods perform poorly on the bridge scene, owing to its symmetrical appearance and repeating geometry. COLMAP and GLOMAP performed best on the Office and Crane scenes, benefiting from the use of a prior assumption of continuous video input.

**Table 4:** Pose accuracy as measured by AUC30 ( $\uparrow$  better) for each scene. Depth Anything 3 and  $\pi^3$  attain the best results, while VGGT performs poorly.

		Office					
Method		V. Low	Low	Med.	High	Crane	Bridge
E2E	Depth Anything 3	0.557	0.560	0.555	0.549	0.223	0.195
	VGGT	0.121	0.126	0.137	0.132	0.043	0.036
	$\pi^3$	0.538	0.537	0.538	0.537	0.272	<b>0.252</b>
SfM	COLMAP	<b>0.916</b>	<b>0.901</b>	<b>0.934</b>	<b>0.951</b>	0.736	0.205
	GLOMAP	0.763	0.709	0.849	0.804	<b>0.849</b>	0.030

**Table 5:** Point cloud Chamfer Distance (m,  $\downarrow$  better) between the ground truth and estimated point clouds. In contrast to the depth map results, COLMAP with known ground truth camera intrinsics and extrinsics outperforms the other methods.

		Office					
Method		V. Low	Low	Med.	High	Crane	Bridge
E2E	DA3 (GT Params.)	0.289	0.290	0.286	0.285	<b>0.307</b>	0.166
	DA3 (Est. Params.)	0.537	0.544	0.540	0.525	0.884	1.043
	VGGT (Est. Params.)	1.070	1.107	0.947	0.922	3.135	3.130
	$\pi^3$ (Est. Params.)	0.780	0.784	0.773	0.785	1.891	1.667
MVS	COLMAP (GT Params.)	<b>0.261</b>	<b>0.255</b>	<b>0.260</b>	<b>0.275</b>	0.526	<b>0.079</b>
	COLMAP (Est. Params.)	0.598	0.571	0.555	0.486	1.026	3.659

## 5.5 Scene Level 3D Reconstruction

All the methods evaluated produce point clouds. In Tab. 5 we present the commonly used chamfer distance and present the F1-score in Tab. 6. Qualitative results of the bridge scene are shown in Fig. 5 and further qualitative results are shown in the supplementary material. From these results, we can see that COLMAP produces point clouds of better or similar accuracy to Depth Anything 3 with or without ground truth camera intrinsics and extrinsics. COLMAP also outperforms the other transformer methods on most scenes except for the crane. Notably, COLMAP demonstrates improved performance with higher soiling settings in the office scene, owing to greater lambertian content on the windows. This is in contrast to the per-view depth estimation results (see Tab. 3), where COLMAP’s performance is the worst of all methods tested. Together, these results suggest that scene-level metrics on point clouds are not appropriate to evaluate the local quality of 3D reconstruction output. This is especially true in an asset inspection or management context where local geometry on a per-view level is important for creating a highly-detailed model.

Consistent with the pose recovery results, we find that transformer-based methods which estimate camera intrinsics and extrinsics produce less accurate point clouds compared to their performance on other benchmarks [28, 52, 57]. Most notably, the point cloud produced by VGGT bears little resemblance to the original structure. This suggests that these transformer-based methods are not well-suited for 3D reconstruction in an asset-inspection context.

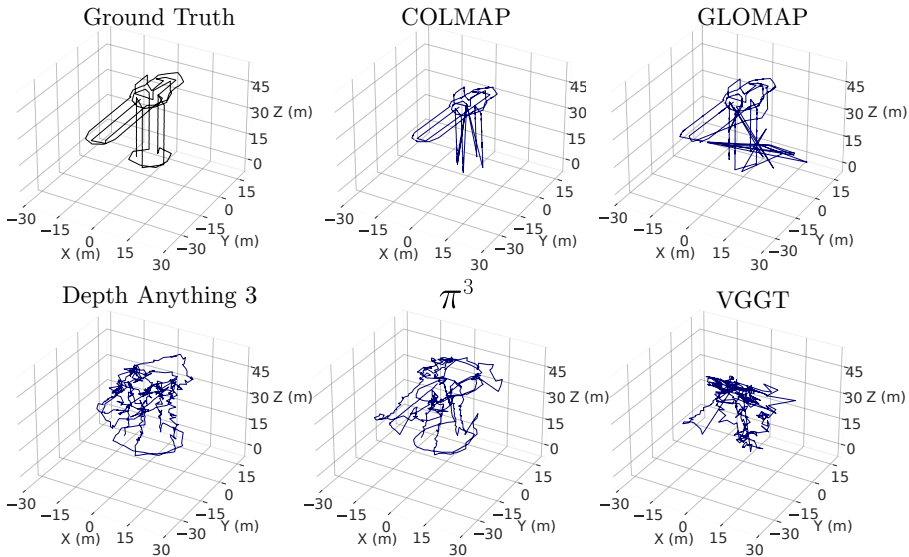


**Fig. 4:** Qualitative camera pose results on the crane scene. COLMAP, GLOMAP, Depth Anything 3 and  $\pi^3$  performed relatively well at estimating the camera poses. However, VGGT performed poorly.

## 6 Conclusion

In this paper, we introduced a novel 3D reconstruction benchmark explicitly designed for the rigorous and specific demands of asset inspection. Unlike existing datasets that rely on distant global capture trajectories, our benchmark provides dense close-proximity capture sequences along with ground truth depth and normal maps. By carefully constructing these environments with complex procedural textures we ensure that algorithms evaluated on our benchmark are forced to handle the photorealistic complexities, including reflections and surface soiling that are unavoidable in actual inspection deployments.

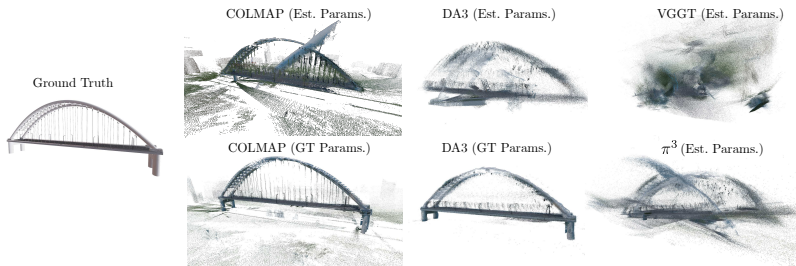


**Fig. 5:** Point clouds from each method on the bridge scene.

**Table 6:** Point cloud F1-score (m, ↓ better) between the ground truth and estimated point clouds. COLMAP achieves superior performance compared to learning based approaches on all scenes except for the crane, where thin features prove difficult to reconstruct reliably.

		Office					
Method		V. Low	Low	Med.	High	Crane	Bridge
E2E	DA3 (GT Params.)	0.243	0.244	0.237	0.236	<b>0.253</b>	0.163
	DA3 (Est. Params.)	0.617	0.625	0.618	0.600	0.744	0.581
	VGGT (Est. Params.)	1.119	1.133	0.913	0.862	1.878	0.966
	$\pi^3$ (Est. Params.)	0.356	0.359	0.353	0.351	0.522	0.463
MVS	COLMAP (GT Params.)	<b>0.187</b>	<b>0.186</b>	<b>0.186</b>	<b>0.185</b>	0.575	<b>0.046</b>
	COLMAP (Est. Params.)	0.646	0.620	0.603	0.544	1.035	3.036

Our evaluation of SfM and MVS pipelines and state-of-the-art transformer based end-to-end methods revealed that state-of-the-art end-to-end 3D reconstruction methods are currently unsuited to an asset inspection context. In this case, the vast numbers of images, taken from close proximity to the asset, with only a small portion of the asset visible in each frame, result in lower performance than on other benchmarks. We also show that global metrics on point clouds are not appropriate to assess local geometric accuracy. Instead, per-view depth metrics are a better choice for this task and are therefore particularly relevant to an asset-inspection context where the high levels of detail are necessary.

Building upon the benchmark established in this paper, future research must pivot toward addressing the limitations of current models. Specifically, this requires the development of novel, memory-efficient architectures capable of natively processing the long continuous image trajectories without relying on offline pose priors. Furthermore, a critical next step involves including the temporal domain to model progressive asset degradation over time, as well as evaluating methods robustness under degraded conditions with noisy telemetry priors. Ultimately, we hope that this dataset will create opportunities for the development of 3D reconstruction methods that are robust and practical for use in asset management.

A link to this dataset and the source files for generating it is included in the supplementary material.

## Acknowledgements

This work was supported in part by the ARC Research Hub in Intelligent Robotic Systems for Real-Time Asset Management (IH210100030), through the the NVIDIA Academic Grant Program and by funding from the Ford Motor Company.

## References

1. Arampatzakis, V., Pavlidis, G., Mitianoudis, N., Papamarkos, N.: Monocular depth estimation: A thorough review. *IEEE Transactions on Pattern Analysis and Ma-*

- chine Intelligence **46**(4), 2396–2414 (Apr 2024) **10**
2. Beche, R., Nedeveschi, S.: ClaraVid: A Holistic Scene Reconstruction Benchmark From Aerial Perspective With Delentropy-Based Complexity Profiling. In: Proceedings of the IEEE/CVF International Conference on Computer Vision. pp. 26015–26025 (2025) **5, 6**
  3. Blender Online Community: Blender - a 3D modelling and rendering package. Blender Foundation (2018), <http://www.blender.org> **2, 7**
  4. Broekman, A., Gräbe, P.J.: PASMVS: A perfectly accurate, synthetic, path-traced dataset featuring specular material properties for multi-view stereopsis training and reconstruction applications. Data in Brief **32**, 106219 (2020) **3, 5, 6**
  5. Chen, K., Yuan, Z., Mao, T., Wang, Z.: Dual-level precision edges guided multi-view stereo with accurate planarization. In: Proceedings of the AAAI Conference on Artificial Intelligence. vol. 39, pp. 2105–2113 (2025) **2**
  6. Crandall, D., Owens, A., Snavely, N., Huttenlocher, D.: Discrete-continuous optimization for large-scale structure from motion. In: CVPR 2011. pp. 3001–3008. IEEE (2011) **3**
  7. Duisterhof, B.P., Zust, L., Weinzaepfel, P., Leroy, V., Cabon, Y., Revaud, J.: MAST3r-SfM: a fully-integrated solution for unconstrained structure-from-motion. In: 2025 International Conference on 3D Vision (3DV). pp. 1–10. IEEE (2025) **4**
  8. Feng, C., Li, H., Gao, F., Zhou, B., Shen, S.: PredRecon: A prediction-boosted planning framework for fast and high-quality autonomous aerial reconstruction. In: 2023 IEEE International Conference on Robotics and Automation (ICRA). pp. 1207–1213. IEEE (2023) **4**
  9. Feng, C., Li, H., Zhang, M., Chen, X., Zhou, B., Shen, S.: FC-planner: A skeleton-guided planning framework for fast aerial coverage of complex 3d scenes. In: 2024 IEEE International Conference on Robotics and Automation (ICRA). pp. 8686–8692. IEEE (2024) **4**
  10. Foi, A.: Clipped noisy images: Heteroskedastic modeling and practical denoising. Signal Processing **89**(12), 2609–2629 (Dec 2009) **8**
  11. Furukawa, Y., Ponce, J.: Accurate, dense, and robust multiview stereopsis. IEEE transactions on pattern analysis and machine intelligence **32**(8), 1362–1376 (2009) **4**
  12. Galliani, S., Lasinger, K., Schindler, K.: Massively parallel multiview stereopsis by surface normal diffusion. In: Proceedings of the IEEE international conference on computer vision. pp. 873–881 (2015) **4**
  13. Gray, J.L., Naman, A.T., Taubman, D.S.: Welsch based multiview disparity estimation. In: 2021 IEEE International Conference on Image Processing (ICIP). pp. 3223–3227 (2021). <https://doi.org/10.1109/ICIP42928.2021.9506766> **10**
  14. Grupp, M.: evo: Python package for the evaluation of odometry and slam. <https://github.com/MichaelGrupp/evo> (2017) **9**
  15. Gu, C., Wei, X., Zeng, Z., Yao, Y., Zhang, L.: IRGS: Inter-reflective gaussian splatting with 2d gaussian ray tracing. In: Proceedings of the Computer Vision and Pattern Recognition Conference (CVPR). pp. 10943–10952 (June 2025) **5**
  16. Guo, Y.C., Kang, D., Bao, L., He, Y., Franc, Y., Zhang, J., et al.: NeRFReN: Neural radiance fields with reflections. In: Proceedings of the IEEE/CVF Conference on Computer Vision and Pattern Recognition. pp. 18409–18418 (2022) **3, 5**
  17. Hartley, R., Zisserman, A.: Multiple view geometry in computer vision. Cambridge university press (2003) **3**
  18. Ihrke, I., Kutulakos, K.N., Lensch, H.P., Magnor, M., Heidrich, W.: Transparent and specular object reconstruction. Computer Graphics Forum **29**(8), 2400–2426 (2010) **3**

19. Jensen, R., Dahl, A., Vogiatzis, G., Tola, E., Aanaes, H.: Large scale multi-view stereopsis evaluation. In: 2014 IEEE Conference on Computer Vision and Pattern Recognition. pp. 406–413. IEEE (2014) [2](#), [5](#), [8](#)
20. Jiang, L., Ren, K., Yu, M., Xu, L., Dong, J., Lu, T., Zhao, F., Lin, D., Dai, B.: Horizon-GS: Unified 3D gaussian splatting for large-scale aerial-to-ground scenes. In: Proceedings of the Computer Vision and Pattern Recognition Conference. pp. 26789–26799 (2025) [5](#)
21. Jiang, Y., Tu, J., Liu, Y., Gao, X., Long, X., Wang, W., Ma, Y.: GaussianShader: 3D gaussian splatting with shading functions for reflective surfaces. In: Proceedings of the IEEE/CVF conference on computer vision and pattern recognition. pp. 5322–5332 (2024) [5](#)
22. Kerbl, B., Kopanas, G., Leimkuehler, T., Drettakis, G.: 3D Gaussian Splatting for Real-Time Radiance Field Rendering. *ACM Transactions on Graphics* **42**(4), 1–14 (Aug 2023) [5](#)
23. Keyang, Y., Qiming, H., Kun, Z.: 3D gaussian splatting with deferred reflection. In: ACM SIGGRAPH Conference Proceedings, Denver, CO, United States, July 28 - August 1, 2024 (2024) [5](#)
24. Knapitsch, A., Park, J., Zhou, Q.Y., Koltun, V.: Tanks and temples: benchmarking large-scale scene reconstruction. *ACM Transactions on Graphics* **36**(4) (jul 2017) [2](#), [5](#)
25. Koch, C., Georgieva, K., Kasireddy, V., Akinci, B., Fieguth, P.: A review on computer vision based defect detection and condition assessment of concrete and asphalt civil infrastructure. *Advanced Engineering Informatics* **29**(2), 196–210 (2015) [2](#)
26. Leroy, V., Cabon, Y., Revaud, J.: Grounding image matching in 3D with MAST3R. In: European conference on computer vision. pp. 71–91. Springer (2024) [4](#)
27. Li, Y., Jiang, L., Xu, L., Xiangli, Y., Wang, Z., Lin, D., Dai, B.: MatrixCity: A large-scale city dataset for city-scale neural rendering and beyond. In: Proceedings of the IEEE/CVF International Conference on Computer Vision. pp. 3205–3215 (2023) [5](#), [6](#)
28. Lin, H., Chen, S., Liew, J.H., Chen, D.Y., Li, Z., Shi, G., Feng, J., Kang, B.: Depth Anything 3: Recovering the visual space from any views. arXiv preprint arXiv:2511.10647 (2025) [2](#), [4](#), [8](#), [10](#), [11](#), [12](#)
29. Lin, L., Liu, Y., Hu, Y., Yan, X., Xie, K., Huang, H.: Capturing, reconstructing, and simulating: the UrbanScene3D dataset. In: European Conference on Computer Vision. pp. 93–109. Springer (2022) [5](#), [6](#)
30. Lindenberger, P., Sarlin, P.E., Larsson, V., Pollefeys, M.: Pixel-perfect structure-from-motion with featuremetric refinement. In: Proceedings of the IEEE/CVF international conference on computer vision. pp. 5987–5997 (2021) [4](#)
31. Lowe, D.G.: Distinctive image features from scale-invariant keypoints. *International journal of computer vision* **60**(2), 91–110 (2004) [3](#)
32. Martell, A., Lauterbach, H.A., Schilling, K., Nuchter, A.: Benchmarking Structure from Motion Algorithms of Urban Environments with Applications to Reconnaissance in Search and Rescue Scenarios. In: 2018 IEEE International Symposium on Safety, Security, and Rescue Robotics (SSRR). pp. 1–7 (Aug 2018), ISSN: 2475-8426 [2](#), [5](#), [6](#)
33. Mildenhall, B., Srinivasan, P.P., Tancik, M., Barron, J.T., Ramamoorthi, R., Ng, R.: NeRF: representing scenes as neural radiance fields for view synthesis. *Communications of the ACM* **65**(1), 99–106 (Jan 2022) [5](#)

34. Mirzazade, A., Popescu, C., Gonzalez-Libreros, J., Blanksvärd, T., Täljsten, B., Sas, G.: Semi-autonomous inspection for concrete structures using digital models and a hybrid approach based on deep learning and photogrammetry. *Journal of Civil Structural Health Monitoring* **13**(8), 1633–1652 (2023) [4](#)
35. Naylor, J., Ila, V., Dansereau, D.G.: Surf-NeRF: Surface regularised neural radiance fields. *arXiv preprint arXiv:2411.18652* (2025) [5](#)
36. Pan, L., Barath, D., Pollefeys, M., Schönberger, J.L.: Global Structure-from-Motion Revisited. In: *European Conference on Computer Vision (ECCV)* (2024) [2](#), [4](#), [5](#), [8](#), [9](#)
37. Sarlin, P.E., DeTone, D., Malisiewicz, T., Rabinovich, A.: SuperGlue: Learning feature matching with graph neural networks. In: *Proceedings of the IEEE/CVF conference on computer vision and pattern recognition*. pp. 4938–4947 (2020) [3](#)
38. Schönberger, J.L., Frahm, J.M.: Structure-from-motion revisited. In: *Conference on Computer Vision and Pattern Recognition (CVPR)* (2016) [3](#), [4](#), [8](#), [9](#)
39. Schönberger, J.L., Zheng, E., Pollefeys, M., Frahm, J.M.: Pixelwise view selection for unstructured multi-view stereo. In: *European Conference on Computer Vision (ECCV)* (2016) [4](#), [8](#)
40. Schöps, T., Schönberger, J.L., Galliani, S., Sattler, T., Schindler, K., Pollefeys, M., Geiger, A.: A multi-view stereo benchmark with high-resolution images and multi-camera videos. In: *Conference on Computer Vision and Pattern Recognition (CVPR)* (2017) [2](#), [5](#), [8](#)
41. Seitz, S.M., Curless, B., Diebel, J., Scharstein, D., Szeliski, R.: A comparison and evaluation of multi-view stereo reconstruction algorithms. In: *2006 IEEE computer society conference on computer vision and pattern recognition (CVPR'06)*. vol. 1, pp. 519–528. IEEE (2006) [5](#)
42. Sharma, A., Kosasih, E., Zhang, J., Brintrup, A., Calinescu, A.: Digital twins: State of the art theory and practice, challenges, and open research questions. *Journal of Industrial Information Integration* **30**, 100383 (2022) [2](#)
43. Smith, N., Moehrle, N., Goesele, M., Heidrich, W.: Aerial path planning for urban scene reconstruction: a continuous optimization method and benchmark. *ACM Transactions on Graphics (TOG)* **37**(6), 1–15 (2018) [4](#), [5](#)
44. Snavely, N., Seitz, S.M., Szeliski, R.: Photo tourism: exploring photo collections in 3d. *ACM Transactions on Graphics (TOG)* **25**(3), 835–846 (2006) [3](#)
45. Strecha, C., Von Hansen, W., Van Gool, L., Fua, P., Thoennessen, U.: On benchmarking camera calibration and multi-view stereo for high resolution imagery. In: *2008 IEEE conference on computer vision and pattern recognition*. pp. 1–8. Ieee (2008) [5](#)
46. T2D2: General Considerations | Data Capture Guide | T2D2 User Documentation (Sep 2023), <https://docs.t2d2.ai/user-guides/data-capture-guide> [2](#), [6](#), [7](#)
47. Tang, J., Gao, Y., Yang, D., Yan, L., Yue, Y., Yang, Y.: DroneSplat: 3D gaussian splatting for robust 3d reconstruction from in-the-wild drone imagery. In: *Proceedings of the IEEE/CVF Conference on Computer Vision and Pattern Recognition*. pp. 833–843 (2025) [5](#)
48. Trendspek: Trendspek capture guide | pro tips for aerial drone surveys & photogrammetry. <https://trendspek.com/resources/capture-guide>, Accessed: 2026-02-20 [2](#), [6](#), [7](#)
49. Umeyama, S.: Least-squares estimation of transformation parameters between two point patterns. *IEEE Transactions on pattern analysis and machine intelligence* **13**(4), 376–380 (2002) [9](#)

50. Verbin, D., Hedman, P., Mildenhall, B., Zickler, T., Barron, J.T., Srinivasan, P.P.: Ref-NeRF: Structured view-dependent appearance for neural radiance fields. *CVPR* (2022) **3, 5**
51. Wang, H., Agapito, L.: 3D reconstruction with spatial memory. In: 2025 International Conference on 3D Vision (3DV). pp. 78–89. IEEE (2025) **10**
52. Wang, J., Chen, M., Karaev, N., Vedaldi, A., Rupprecht, C., Novotny, D.: VGGT: Visual geometry grounded transformer (2025) **2, 4, 8, 11, 12**
53. Wang, J., Rupprecht, C., Novotny, D.: PoseDiffusion: Solving pose estimation via diffusion-aided bundle adjustment (2023) **10**
54. Wang, J., Hu, Q., Bao, C., Zhu, Y., Bao, H., Cui, Z., Zhang, G.: LightCity: An urban dataset for outdoor inverse rendering and reconstruction under multi-illumination conditions. In: Proceedings of the IEEE/CVF International Conference on Computer Vision. pp. 26477–26487 (2025) **5, 6**
55. Wang, Q., Zhang, Y., Holynski, A., Efros, A.A., Kanazawa, A.: Continuous 3D perception model with persistent state. In: *CVPR*. pp. 10510–10522 (2025) **10**
56. Wang, S., Leroy, V., Cabon, Y., Chidlovskii, B., Revaud, J.: DUS3R: Geometric 3D vision made easy. In: Proceedings of the IEEE/CVF conference on computer vision and pattern recognition. pp. 20697–20709 (2024) **4**
57. Wang, Y., Zhou, J., Zhu, H., Chang, W., Zhou, Y., Li, Z., Chen, J., Pang, J., Shen, C., He, T.:  $\pi^3$ : Permutation-Equivariant Visual Geometry Learning. arXiv preprint arXiv:2507.13347 (2025) **2, 4, 8, 10, 11, 12**
58. Wang, Y., Wan, S., Qiu, R., Li, X.: A path planning algorithm for UAV 3d surface inspection based on normal vector filtering and integrated viewpoint evaluation. *Journal of Field Robotics* **42**(6), 2561–2579 (2025) **4**
59. Xu, Z., Chen, B., Zhan, X., Xiu, Y., Suzuki, C., Shimada, K.: A vision-based autonomous UAV inspection framework for unknown tunnel construction sites with dynamic obstacles. *IEEE Robotics and Automation Letters* **8**(8), 4983–4990 (2023) **4**
60. Yao, Y., Luo, Z., Li, S., Zhang, J., Ren, Y., Zhou, L., Fang, T., Quan, L.: Blended-MVS: A large-scale dataset for generalized multi-view stereo networks. *Computer Vision and Pattern Recognition (CVPR)* (2020) **2, 5, 6, 8**
61. Zeng, Z., Wang, Y., Guan, T.: Matching ambiguity-resilient multi-view stereo via adaptive patch deformation. *Pattern Recognition* p. 112593 (2025) **2**
62. Zheng, E., Dunn, E., Jovic, V., Frahm, J.M.: PatchMatch based joint view selection and depthmap estimation. In: Proceedings of the IEEE conference on computer vision and pattern recognition. pp. 1510–1517 (2014) **4**

## A Dataset

The full dataset can be accessed here: <https://huggingface.co/datasets/Slighting3121/3D-Reconstruction-Benchmark-Asset-Inspection>. This repository contains all the images, depth maps, and mesh models used in the evaluation. Additionally, .blend files have been included to allow one to modify these scenes or create new ones.

### A.1 Blender Scene Details

To make the scenes, we primarily used open source resources made by artists available on the BlenderKit platform: [www.blenderkit.com](http://www.blenderkit.com). All assets from

BlenderKit have an RF or CC0 license. These resources include materials, models, and HDRis, which are listed below:

1. Cosmo — [Suspension/Arch Bridge](#)
2. MapacheDRelease — [Crane Tower](#)
3. Mohammadi, S. — [Realistic Procedural Grass \(Cycles/Eevee\)](#)
4. Godoi, M. — [Procedural Concrete](#)
5. Russo 3D — [Procedural Brick](#)
6. Middleton, J. — [Bricks Procedural Wall](#)
7. Middleton, J. — [Brick Wall Procedural](#)
8. FreePoly — [Over The Construction Site Yellow Mud](#)
9. FreePoly — [Lake Highsky Blue Sky](#)
10. Mirazev, A. — [Modern Building](#)
11. Jacinto, M. et al. — [Iris Drone Model](#)
12. Se-Cam, J. — [80s Cartoon Wagon Car](#)
13. Se-Cam, J. — [Cartoon Car / Toy Car](#)
14. Se-Cam, J. — [80s Cartoon Pick-Up](#)
15. Tirindelli, D. — [6kw Solar Panels Structure](#)
16. Rexodus — [Antenna](#)
17. Mitroi, R. — [AC Unit Big](#)
18. Wells, C. — [Procedural Concrete Tiles](#)
19. Paludo, L. — [Simple Concrete Procedural](#)
20. Share Textures — [Dark Steel](#)
21. Michaud, A. — [Textured Painted Wall \(Procedural\)](#)
22. Yang, R. — [White Wall 02](#)
23. Adhe, E. — [Black Painted Plaster Wall](#)
24. Pambudi, R.R. — [Material Window Glass Cycle](#)
25. Yang, R. — [Urban City Highsky Bluesky](#)
26. NK Productions — [Asphalt Road Procedural](#)

The Iris Drone Model is from a GitHub project with a [BSD 3-Clause License](#).

Below, we describe how we use each asset to produce each scene:

*Office building* This scene features an office building (10) and stylised cars (13, 12, 14). We added solar panels (15), air conditioning units (17) and an antenna (16) to the roof of the building for extra detail. The building is placed on a tiled concrete ground plane, which is procedurally generated (18). There is also a road consisting of procedurally generated asphalt (26). To ensure that the building had sufficiently detailed and realistic textures, we modified the original textures of the model. The roof was changed to procedurally generated concrete (19); the walls were set to procedurally generated painted walls (21) and a non-repeating white wall texture walls (22); window borders and fences were set to painted steel (20); and the window glass was based on (24). Particular attention was paid to the window glass; noise was added to the normals of the windows to simulate the slightly warped reflections present in real windows. Furthermore, the soiling settings were achieved via adjusting the strength of a noise texture which changed the roughness of the glass. The different soiling settings are shown in Fig. 6. Several representative frames from this scene are shown in Fig. 7.

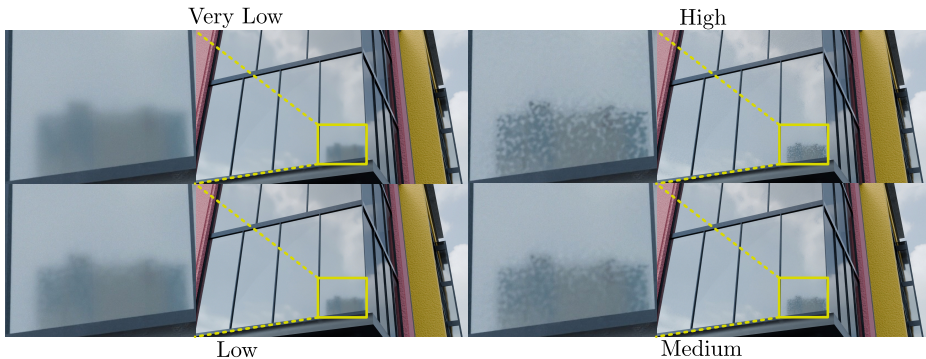


**Fig. 6:** The same frame of the office building scene with the four different soiling settings.



**Fig. 7:** Representative frames from the office building scene.

*Crane* This scene features a tall tower crane (2) on a procedurally generated concrete floor (4). An HDRi of a construction site (8) was employed as an environment map. Several frames from this scene are shown in Fig. 8.

*Bridge* This scene features a long tied arch bridge (1) on a procedurally generated grass floor (3). An HDRi of a city crossed by a river (9) was employed as an environment map. Several frames from this scene are shown in Fig. 9. For both the Bridge and the Crane scenes, we added rectangular prisms surrounding the asset to be inspected. These are made of three variations of bricks: red bricks (5), yellow bricks (6), and white bricks (7). This was done to simulate structures in the background of the crane and the bridge.

## B Hardware Details

COLMAP reconstructions were performed on a workstation with an NVIDIA GeForce RTX4070, an Intel Core i7-14700, and 32GB RAM. All other methods were evaluated on a dedicated compute server equipped with an NVIDIA



**Fig. 8:** Representative frames from the crane scene.

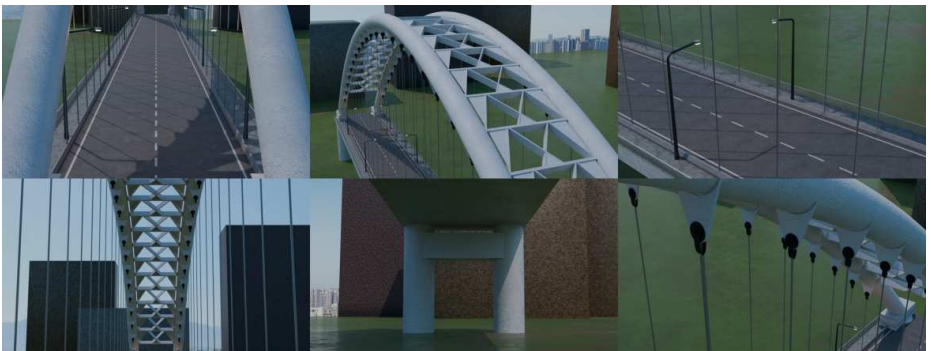


**Fig. 9:** Representative frames from the bridge scene.

RTX6000 Ada Generation GPU, an AMD Ryzen 9 9950X processor, and 128GB RAM.

## C Baseline Method Parameters

### C.1 Traditional Reconstruction Approaches

When reconstructing a scene using COLMAP or GLOMAP, there are many options one can select at each stage.

When we provided COLMAP with the ground truth camera intrinsics and extrinsics for the sparse reconstruction, we used the following stages with their default parameters:

- feature\_extractor
- exhaustive\_matcher
- point\_triangler

When COLMAP estimates its own parameters, we use the automatic reconstructor, with default settings unless except for:

- `automatic_reconstructor`
  - `camera_model`: `SIMPLE_PINHOLE`
  - `single_camera`: `1`
  - `dense`: `0`
  - `gpu_index`: `1`
  - `use_gpu`: `1`
  - `data_type`: `video`
  - `quality`: `medium`

For the sparse GLOMAP reconstruction, we use the GlobalMapper stage with default parameters, using the database produced by the automatic reconstructor with the aforementioned parameters.

For the subsequent dense reconstruction stage, we used the following stages with default parameters unless otherwise indicated:

- `image_undistorter`
- `patch_match_stereo`:
  - `geom_consistency`: `false`
  - `filter`: `true`
  - `max_image_size`: `480`
- `stereo_fusion`:
  - `max_image_size`: `480`
  - `input_type`: `photometric`

## C.2 End-to-End Methods

We evaluate three models: VGGT, Depth Anything 3, and  $\pi^3$ . In all cases, inference is performed in non-overlapping batches, where the batch size corresponds to the maximum number of images that can be processed by the respective model on a single NVIDIA RTX 6000 GPU. For VGGT (“VGGT-1B”), we use batches of 200 images. For Depth Anything 3 (“DA3NESTED-GIANT-LARGE”), we use batches of 400 images and evaluate two variants: one given ground truth poses and one without ground truth poses. For  $\pi^3$ , we use batches of 100 images. For all methods, point maps are converted to point clouds using only points with confidence greater than 0.75.

## D Evaluation Metrics

To comprehensively assess the performance of the evaluated methods, we measure depth map accuracy, camera pose accuracy, registration completeness, focal length accuracy, and point cloud fidelity. In this section, we detail each metric we use.

*Depth Map Accuracy* To evaluate depth maps, we use the scale-invariant mean squared error (sRMSE). In uncalibrated monocular reconstructions and end-to-end pipelines, depth predictions often exhibit an arbitrary global scale. We employ sRMSE to ensure that this scale ambiguity does not penalise the underlying geometric accuracy of the depth maps. The sRMSE is defined by:

$$\text{sRMSE}(\log) = \frac{1}{V} \sum_{p \in \mathcal{V}} (\log d_{\text{gt}}(p) - \log d_{\text{est}}(p) + a(d_{\text{gt}}, d_{\text{est}}))^2, \quad (1)$$

where  $a(d_{\text{gt}}, d_{\text{est}}) = \frac{1}{V} \sum_{p \in \mathcal{V}} (\log d_{\text{est}}(p) - \log d_{\text{gt}}(p))$  is the scale alignment value  $d_{\text{gt}}$  and  $d_{\text{est}}$  are the ground truth and estimated depth maps respectively, and  $\mathcal{V}$  is the set of valid pixels.

*Camera Pose Accuracy* We use the Area under Curve (AUC) to evaluate the camera pose accuracy. The AUC is defined by,

$$\text{AUC} = \sum_{\tau \in [1, 30]} \min(\text{RRA}@ \tau, \text{RTA}@ \tau), \quad (2)$$

where RTA and RRA refer to the relative translation accuracy and relative rotation accuracy, respectively. For a given error threshold  $\tau$ , the  $\text{RRA}@ \tau$  and  $\text{RTA}@ \tau$  represent the percentage of all camera pairs  $(i, j)$  whose errors fall strictly below  $\tau$ . The relative translation error  $\text{RTA}_{i,j}$  between camera pose  $i$  and  $j$  is defined by,

$$\text{RTA}_{i,j} = \arccos \left( \frac{\mathbf{t}_{ij}^\top \mathbf{t}_{ij}^*}{\|\mathbf{t}_{ij}\| \|\mathbf{t}_{ij}^*\|} \right). \quad (3)$$

The  $\text{RRA}_{i,j}$  is defined as the angle between the estimated relative rotation  $R_i R_j^T$  and the ground truth relative rotation  $R_i^* (R_j^*)^T$ . A higher AUC indicates that a method reliably produces poses with minimal error bounds, making it a robust single-value summary of trajectory quality.

*Registration Rate* Some methods discard frames with low feature matches or high uncertainty, resulting in an incomplete set of poses. Evaluating the accuracy strictly on a successful subset can significantly increase the score of a method by ignoring the challenging frames on which it failed. To account for this, we evaluate only valid estimated poses and report the registration rate, defined as the proportion of successfully estimated camera poses relative to the total number of images in the sequence.

*Point Cloud Accuracy* To evaluate the fidelity of the reconstructed 3D point clouds, we use the chamfer distance (CD) and the F1-score. The chamfer distance is defined by

$$\text{CD}(\mathcal{R}, \mathcal{G}_p) = \frac{1}{|\mathcal{R}|} \sum_{\mathbf{r} \in \mathcal{R}} e_{\mathbf{r} \rightarrow \mathcal{G}_p} + \frac{1}{|\mathcal{G}_p|} \sum_{\mathbf{g} \in \mathcal{G}_p} e_{\mathbf{g} \rightarrow \mathcal{R}}, \quad (4)$$

where  $e_{\mathbf{r} \rightarrow \mathcal{G}_p}$  refers to the distance between an estimated or reconstructed point  $\mathbf{r}$  in the set of reconstructed points  $\mathcal{R}$  and the ground truth set of points  $\mathcal{G}_p$ . Specifically,

$$e_{\mathbf{r} \rightarrow \mathcal{G}_p} = \min_{\mathbf{g} \in \mathcal{G}_p} \|\mathbf{r} - \mathbf{g}\|_2. \quad (5)$$

The chamfer distance adds both the accuracy,

$$\text{Acc}(\mathcal{R}, \mathcal{G}_p) = \frac{1}{|\mathcal{R}|} \sum_{\mathbf{r} \in \mathcal{R}} e_{\mathbf{r} \rightarrow \mathcal{G}_p}, \quad (6)$$

and the completeness,

$$\text{Comp}(\mathcal{R}, \mathcal{G}_p) = \frac{1}{|\mathcal{G}_p|} \sum_{\mathbf{g} \in \mathcal{G}_p} e_{\mathbf{g} \rightarrow \mathcal{R}}. \quad (7)$$

By considering both the accuracy and the completeness, the chamfer distance can only be minimised by a point cloud that contains points that are highly accurate and cover all the ground truth points.

Similarly, the F1-score combines both the accuracy and completeness using the harmonic mean between them. Specifically,

$$\text{F1}(\mathcal{R}, \mathcal{G}_p) = \frac{2\text{Acc}(\mathcal{R}, \mathcal{G}_p) \cdot \text{Comp}(\mathcal{R}, \mathcal{G}_p)}{\text{Acc}(\mathcal{R}, \mathcal{G}_p) + \text{Comp}(\mathcal{R}, \mathcal{G}_p)}. \quad (8)$$

## E Additional Evaluation Results

*Camera Intrinsic*s We include the mean relative error (MRE) in the estimated focal length in Tab. 7. MRE is calculated as,

$$I(\mathcal{C}, f_{\mathbf{gt}}) = \frac{1}{|\mathcal{C}|} \sum_{\mathbf{c} \in \mathcal{C}} \frac{|f_{\mathbf{c}} - f_{\mathbf{gt}}|}{f_{\mathbf{gt}}}, \quad (9)$$

where  $f_{\mathbf{gt}}$  is the ground truth focal length,  $f_{\mathbf{c}}$  is the estimated focal length for view  $\mathbf{c}$  of the set of estimated views  $\mathcal{C}$ . In COLMAP and GLOMAP’s case, the set size is 1.

From these results, we see that the SfM methods perform substantially better on all scenes, with COLMAP outperforming GLOMAP. DA3 outperforms VGGT across all scenes, while still falling far behind the SfM methods. This improved performance is because SfM approaches are much more constrained. They allow the user to specify additional priors on the camera intrinsics, including the camera model used and whether each image is taken with the same camera. Note that shared camera intrinsics between frames is a realistic assumption in many situations, such as video data. Furthermore, a user can be expected to know whether or not this applies in a given scene.

**Table 7:** Mean relative error in focal length(pixels) (%  $\downarrow$  better). Due to DA3 and VGGT outputting per frame intrinsics we perform a mean. For COLMAP and GLOMAP only a single intrinsics is estimated and compared to. Note that  $\pi^3$  does not output any camera intrinsics.

		Office					
Method		V. Low	Low	Med.	High	Crane	Bridge
	DA3	11.629	11.630	11.220	11.090	6.953	6.090
E2E	VGGT	19.209	18.927	18.221	18.047	8.415	9.776
	$\pi^3$	—	—	—	—	—	—
SFM	COLMAP	<b>0.009</b>	0.103	0.134	0.047	<b>0.017</b>	<b>0.144</b>
	GLOMAP	0.051	<b>0.022</b>	<b>0.044</b>	<b>0.011</b>	0.098	0.436

**Table 8:** The percentage (%) of registered poses ( $\uparrow$  better).

		Office					
Method		V. Low	Low	Med.	High	Crane	Bridge
	COLMAP	71.03	69.41	69.16	69.24	79.91	84.82
	GLOMAP	<b>76.70</b>	<b>74.93</b>	<b>74.57</b>	<b>73.55</b>	<b>90.34</b>	<b>97.02</b>

*Registration Rate* All of the transformer-based methods that we evaluated produced a complete set of camera poses. However, COLMAP and GLOMAP dropped views that did not converge. For each scene, we report the percentage of views that COLMAP and GLOMAP actually estimated the pose for in Tab. 8. We can clearly see that GLOMAP reports a higher proportion of registered poses.

*Qualitative Depth Map Results* Additional qualitative depth map results are shown in Fig. 10 and Fig. 11. Learning-based methods significantly outperform COLMAP in these frames. Note that the transformer-based methods often misestimate the depth of the background and sometimes blur together portions of the truss structures.

*Qualitative Poses Results* Additional qualitative camera pose estimation results are shown in Fig. 12 and Fig. 13. From these results, we can see that all methods perform very poorly on the bridge scene. However, on the office building scene, COLMAP performs the best, followed by (in order) GLOMAP, Depth Anything 3,  $\pi^3$  and VGGT.

*Qualitative Point Cloud Results* Additional point cloud plots are shown in Fig. 14 and Fig. 15. COLMAP and Depth Anything 3 produce accurate point clouds of the office building scene, especially when the ground truth camera intrinsics and extrinsics are provided. However, COLAMP does not place points in the windowed areas, and Depth Anything 3 does.  $\pi^3$  produces a much less accurate point cloud, and VGGT produces a misaligned output.

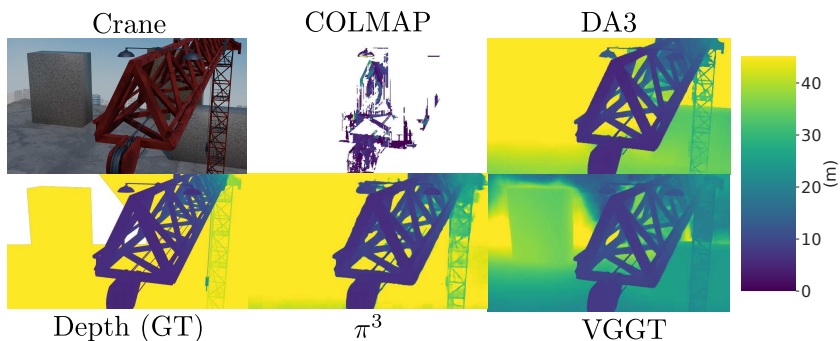


**Fig. 10:** Depth maps on the crane scene using self-estimated parameters. Each depth map is scaled to match the ground truth range, with near-far corresponding to blue-yellow. COLMAP is unable to estimate the majority of the frame accurately, whereas transformer-based methods demonstrate good performance in the foreground. However, in the background, performance degrades.

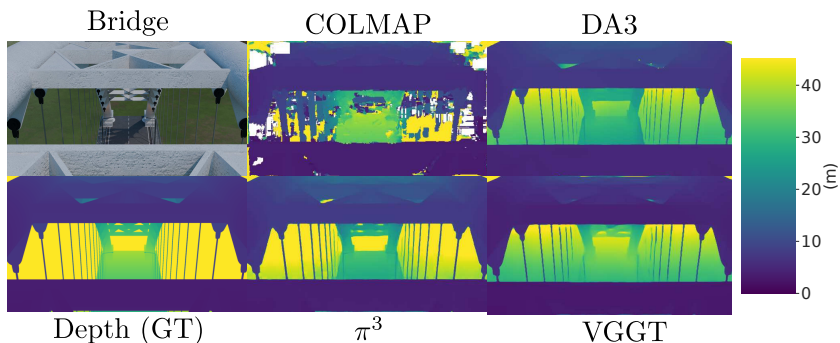


**Fig. 11:** Depth maps on the bridge scene using self-estimated parameters. Each depth map is scaled to match the ground truth range, with near-far corresponding to blue-yellow. COLMAP performs relatively well on the road surface of the bridge and in the foreground, but the suspension cables are estimated to be far too thick. the learning based methods capture the shape of the bridge from this view, but perform poorly in the background.

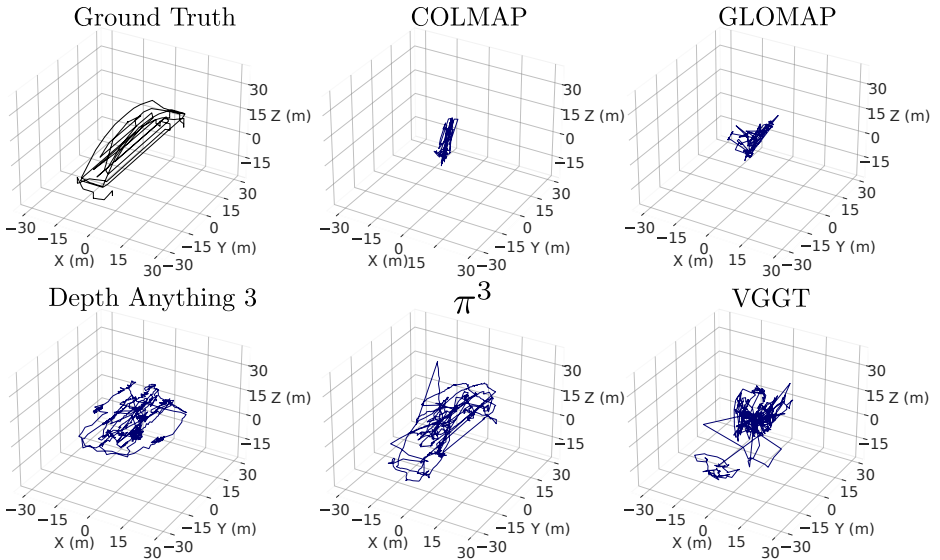


**Fig. 12:** Camera pose results on the bridge scene. All methods perform poorly.

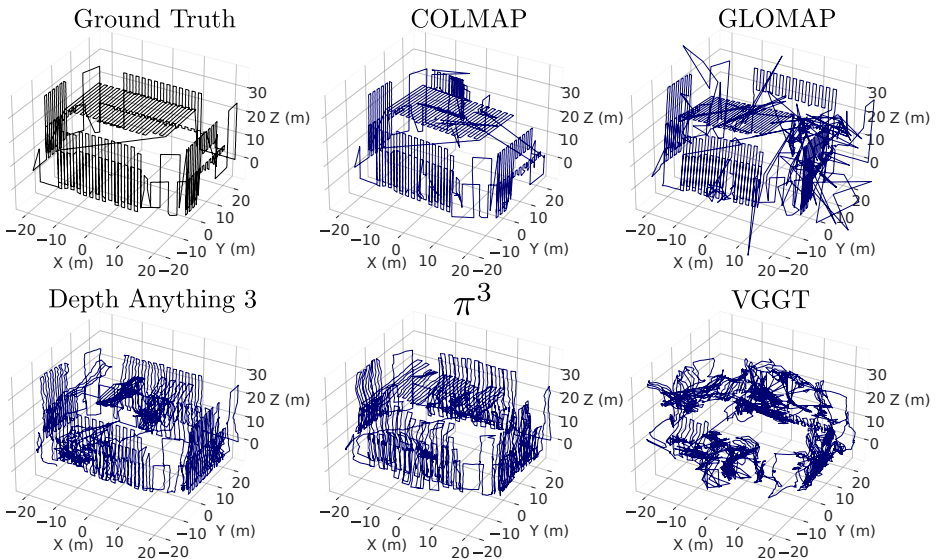


**Fig. 13:** Camera pose results on the office scene with the very low soiling setting. COLMAP performed best, followed by (in order) GLOMAP, Depth Anything 3,  $\pi^3$  and VGGT.

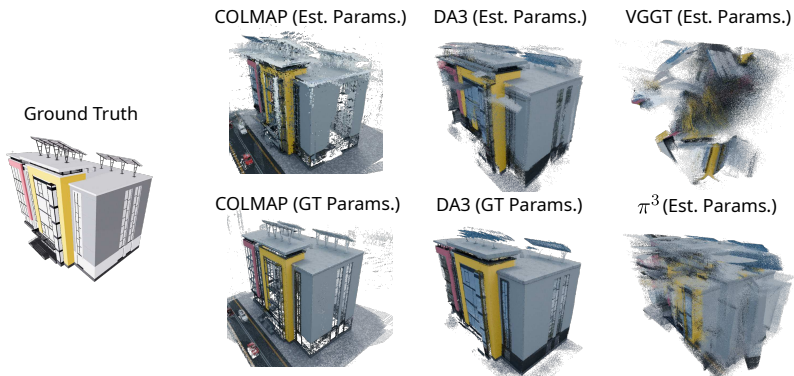


**Fig. 14:** Point clouds of the office building with very low soiling settings. Depth Anything 3 and COLMAP produce the most accurate point clouds. Note that COLMAP does not place points in the windowed areas, whereas Depth Anything 3 does.  $\pi^3$  is somewhat misaligned, and VGGT is strongly misaligned.

In the crane scene, COLMAP produces a very sparse but accurate point cloud regardless of whether or not the ground truth camera intrinsics and extrinsics are provided. Depth Anything 3 produces a dense point cloud, which has significant noise when the ground truth camera intrinsics and extrinsics are provided. Without these parameters, the reconstructed crane is missing large parts of the vertical truss and is significantly noisier. Once again,  $\pi^3$  produces misaligned output. Surprisingly, VGGT produces a point cloud that is unrecognisable as a crane.

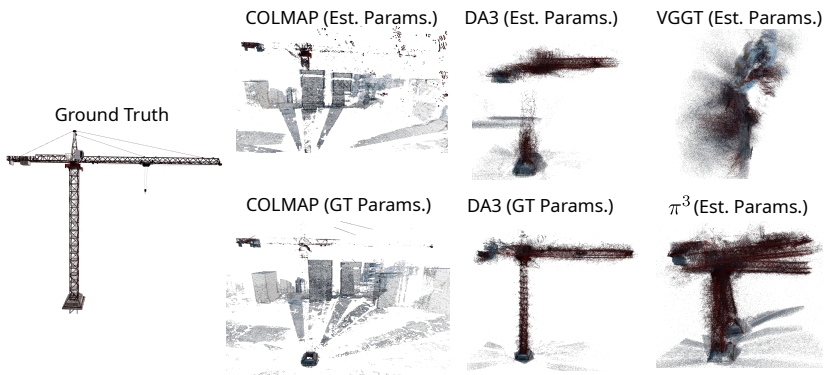


**Fig. 15:** Point clouds of the crane scene. COLMAP produces very sparse outputs of the crane, mainly reconstructing the background, whereas the other methods mainly reconstruct the crane, with varying degrees of accuracy. Depth Anything 3 produces the most accurate point clouds, while  $\pi^3$  is somewhat misaligned. VGGT produces unrecognisable output.